

A New Three-Dimensional Microstructure-Resolved Model to Assess Mechanical Stress in Solid-State Battery Electrodes

Siwar Ben Hadj Ali, Mohammed Alabdali, Virginie Viallet, Vincent Seznec, and Alejandro A. Franco*

In all-solid-state batteries (ASSBs), the mechanical stress generated during electrode (de)lithiation plays a critical role in determining the cell longevity because of the induced degradation mechanisms. This stress originates from local volume fluctuations in the active electrode materials, such as nickel-rich $\text{LiNi}_x\text{Mn}_{1-x}\text{Co}_z\text{O}_2$, which are intrinsically coupled to spatial variations in lithium-ion concentration during electrochemical cycling. Herein, a novel ASSB model that considers electrochemistry and solid mechanics in a one-way coupled manner is presented. The model spatially resolves 3D-microstructure of an ASSB half-cell generated from wet manufacturing process simulations and is based on linear continuum mechanics. The coupling of electrochemistry and solid

mechanics is incorporated via lithiation-dependent volumetric changes of the active material and the microstructural changes due to deformed geometries affecting the particles percolation paths. Furthermore, it is shown that the overall volume change of the half-cell is dependent on the C-rate and on the applied stack pressure. Finally, the findings demonstrate that solid-mechanical effects and their interplay with electrochemical phenomena significantly impact the evolution of interfacial surface area and the total pore volume. These factors are crucial for ensuring accurate computational predictions, underscoring the necessity of incorporating such interactions in battery modeling approaches.

1. Introduction

Lithium-ion batteries (LIBs) play a pivotal role in various energy storage applications, ranging from stationary storage systems to electric and hybrid vehicles. However, the energy density and fast-charging capability of conventional LIBs are approaching fundamental physical limits.^[1] In response, all-solid-state batteries (ASSBs) have emerged as a promising next-generation technology, offering higher energy and power densities while simultaneously

addressing critical safety concerns associated with liquid electrolytes, such as thermal runaway and pressure build-up.^[2,3] Despite these advantages, several technological challenges remain that hinder the widespread commercialization of ASSBs.

One of the key challenges arises from the intrinsic solid-state nature of all components in ASSBs. The active material (AM) undergoes volume changes during (de)lithiation, which results in strong interactions between electrochemical and mechanical processes in the absence of liquid-phase buffering.^[4,5–6] These interactions introduce mechanical stresses, interfacial degradation, and contact losses, all of which can severely impact electrochemical performance. As a result, single-field investigations, focusing solely on electrochemistry or solid mechanics, are not sufficient to capture the full complexity of these systems (**Figure 1**).^[7]

A growing number of ex situ,^[8] in situ,^[9] and in-operando^[10] experimental studies have aimed to elucidate the interplay between electrochemistry and solid mechanics in ASSBs. Given that many of the critical physical phenomena in ASSBs are not directly observable, researchers employ a combination of advanced characterization techniques.^[11,12–13] However, these experimental methods are often expensive, time-consuming, or inaccessible to a large portion of the research community. Furthermore, even with state-of-the-art characterization tools, critical open questions remain regarding the mechanistic coupling of electrochemistry and mechanics.

To address these limitations, numerical simulations are increasingly recognized as powerful tools for investigating the complex interplay of mechano-electrochemical phenomena in ASSBs. Yet, due to the high complexity of these interactions, many existing computational approaches rely on simplifications, either by

S. Ben Hadj Ali, M. Alabdali, V. Viallet, V. Seznec, A. A. Franco
Laboratoire de Réactivité et de Chimie des Solides
UMR CNRS 7314
Université de Picardie Jules Verne
80039 Amiens Cedex, France
E-mail: alejandro.franco@u-picardie.fr

S. Ben Hadj Ali, M. Alabdali, V. Viallet, V. Seznec, A. A. Franco
Réseau sur le Stockage Electrochimique de l'Energie (RS2E)
Hub de l'Energie, FR CNRS, 15 rue Baudelocque, 80039 Amiens, France

S. Ben Hadj Ali, V. Seznec, A. A. Franco
ALISTORE-European Research Institute
Hub de l'Energie, FR CNRS 3104, 15 Rue Baudelocque, 80039 Amiens, France

A. A. Franco
Institut Universitaire de France
103 boulevard Saint Michel, 75005 Paris, France

 Supporting information for this article is available on the WWW under <https://doi.org/10.1002/batt.202500540>
 © 2025 The Author(s). *Batteries & Supercaps* published by Wiley-VCH GmbH. This is an open access article under the terms of the Creative Commons Attribution License, which permits use, distribution and reproduction in any medium, provided the original work is properly cited.

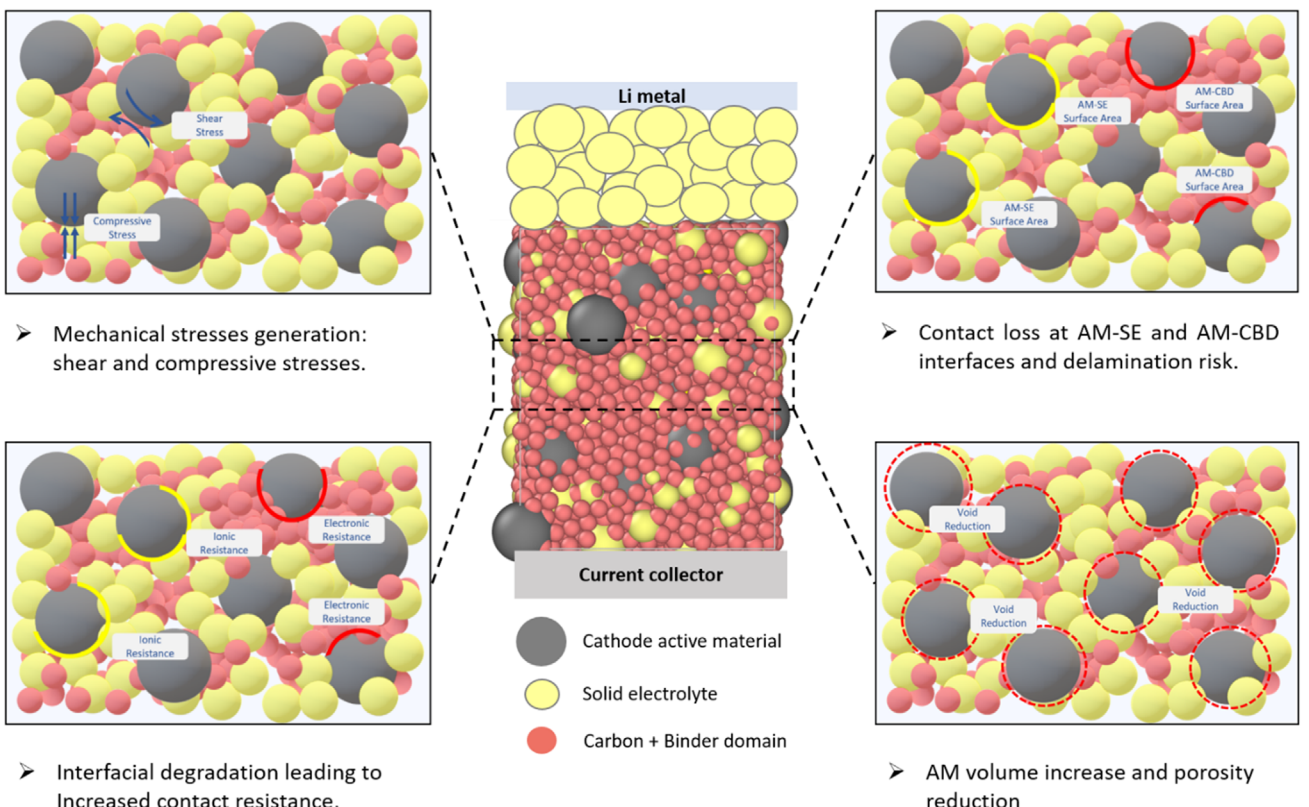


Figure 1. Possible mechanical phenomena at the contact area between the AM and SE or CBD in ASSB composite positive electrodes.

reducing the scope of physical interactions considered or by employing idealized geometries. Consequently, many models fail to provide reliable predictions or quantitative insights into the underlying physical processes.

Recent studies have proposed microstructure-resolved models that describe electrochemical processes in ASSB but these often neglect solid mechanics.^[14–16] Others incorporate both electrochemistry and solid mechanics but rely on linear elasticity assumptions,^[17–24,25] which may not be valid for materials that experience volume changes exceeding several hundred percent during full lithiation.^[26,27] Additionally, some studies adopt advanced modeling frameworks but are constrained to simplified geometries,^[28–30,31] such as 1D configurations,^[32] 2D representations,^[33,34] or single-particle analyses,^[35–37] thereby overlooking crucial local heterogeneities in current density, lithium concentration, and mechanical stress distributions. However, 3D mesoscale simulations of ASSB composite electrodes based on realistic microstructures derived from manufacturing process modeling and incorporating coupled electrochemical-mechanical behavior, remain unavailable. To the best of our knowledge, our work presented in this article represents the first attempt. A few related efforts can be found in the literature, including a study employing the Discrete Element Method (DEM) for silicon-based systems,^[38] a phase-field modeling approach restricted to 2D-domains,^[39] and another DEM-based study by our group that focused on analyzing mechanical stresses after electrochemical cycling (**Table 1**).^[40]

In this study, we present a novel computational framework that provides a comprehensive analysis of the

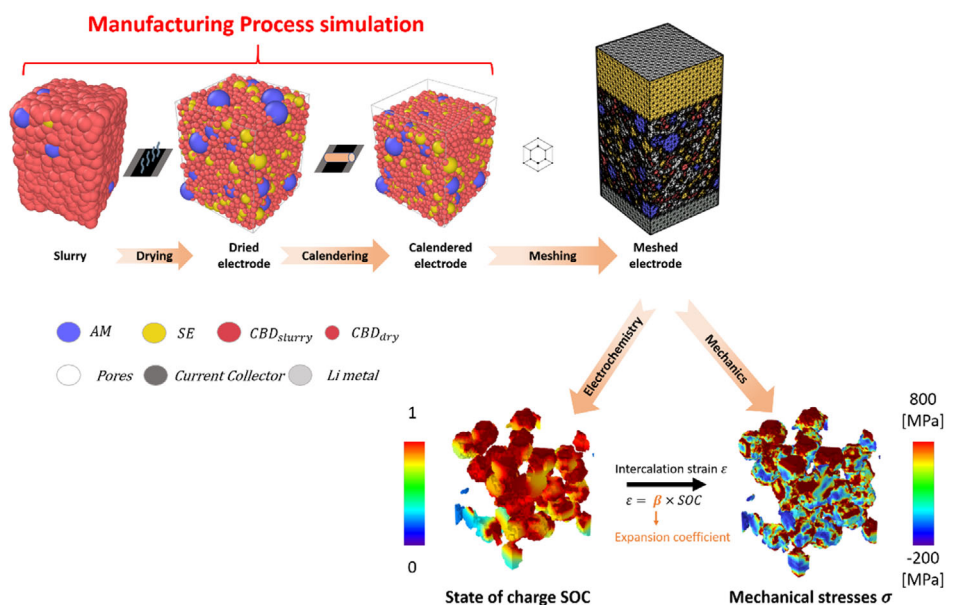
electrochemical-mechanical coupling in ASSBs. Specifically, we develop a 3D finite element model based on a linear continuum mechanics formulation. This model uniquely integrates a calendered microstructure generated from wet manufacturing process simulations, enabling the resolution of local physical phenomena without spatial homogenization. Importantly, the model employs a one-way coupling approach, where electrochemistry drives mechanical deformations, while the mechanical field does not influence the electrochemical behavior.

2. 3D-Resolved Microstructure Generation

This study involves an electrode microstructure that was previously generated and reported^[41] and further analyzed electrochemically in our own recent publication.^[16] The wet (solvent-based) fabrication of NMC-based composite electrodes was conducted experimentally, and based on the experimental characterization of the associated slurries and the resulting porous composites, a predictive computational model was constructed to simulate the 3D slurry-based manufacturing process of ASSB electrodes.^[41,42] This was achieved using coarse-grained molecular dynamics (CGMD) simulations implemented in the LAMMPS software package.^[43] The simulated wet manufacturing process consists of three key stages: slurry preparation, drying, and calendering (**Figure 2**). The model incorporates a microstructure of AM, Li₆PS₅Cl as solid electrolyte (SE), and carbon-binder-solvent domains with a weight formulation of AM:SE:CBD = 69:27.55:3.45, AM particle size of

Table 1. Comparative overview of some state of the art physics-based modeling studies on battery electrodes.

Study	Numerical method	System	Dimension	Plasticity	Origin of the microstructure	Carbon and binder explicit presence	Irregular particle shape
This study	FEM	Solid-state lithium ion battery	3D	No	Manufacturing simulation of composite cathode	Yes	Yes
[18]	Phase-field	Lithium-ion battery	3D	Yes	X-ray computed tomography (CT) imaging	Yes	Yes
[25]	Phase-field	Sodium-ion battery	1D/2D	No	Single idealised particle	No	No
[69]	FEM	Solid-state lithium ion battery	3D	Yes	Homogeneous electrode	No	No
[64]	FEM + phase-field	Solid-state lithium ion battery	2D	Yes	Scanning-electron-microscopy (SEM)	No	Yes
[38]	DEM	Solid-State-lithium ion Silicon-based	3D	Yes	Stochastically-generated	Yes	No
[39]	Phase-field	Solid-State-lithium ion Silicon-based	2D	Yes	SEM	No	Yes


Figure 2. Our simulation workflow of ASSBs composite cathodes: from the wet manufacturing process (slurry to calendered electrode) followed by the half-cell mechano-electrochemistry assessment.

10 µm and ≈12% porosity, however, it does not explicitly differentiate between the carbon and binder components. The CGMD methodology employs force fields that capture interparticle interactions and mechanical behavior, which were calibrated to match experimental observations.

During the transition from slurry to the dried electrode, the carbon-binder-solvent domains shrink to represent solvent evaporation and leading to the formation of the carbon-binder domain (CBD). The calendering process is modeled by applying a uniform downward displacement to the top boundary, compressing the electrode while the bottom surface remains fixed. Further details regarding the simulation of the slurry and drying steps can be found in our earlier works.^[44,45] Subsequently, we developed an electrochemical model^[16] that solves charge transport and interfacial kinetics equations for electrode microstructures predicted from the wet manufacturing process. This

model captures how increased calendering degree, corresponding to the reduction in electrode thickness from the calendering process, reduces lithium concentration gradients, reaction overpotentials, and ionic bottlenecks within the NMC cathode. However, mechanical effects were not considered in that model, particularly the lithiation-induced volume expansion of NMC811 particles, which limits the model's physical fidelity.

To address this limitation, the present work, illustrated in Figure 2, extends our pre-existing electrochemical framework^[16] by incorporating the lithiation-dependent volumetric expansion of NMC811 during a single discharge, thereby enabling coupled electrochemical-mechanical analysis. This approach allows us to investigate the evolution of mechanical stresses arising from volume changes during the lithiation in an NMC cathode of ASSB half-cell. Specifically, we focus on a microstructure with 20% calendering degree

3. Simulation Outline

3.1. From Discrete to Continuum Modeling

A specific postprocessing step, involving voxelization, performed on the CGMD simulation data was developed to transform the particles from spherical to irregular shapes in our continuum model implemented by using the Finite Element Method (FEM). During this step, overlaps between CBD and AM or between CBD and SE are handled based on adjusting the volume calculations by reducing the volume attributed to the CBD and adding this reduced volume to the AM or SE, respectively. This adjustment implicitly considers the porosity of the CBD by reducing its presence in overlapping regions, as one knows that CBD can be porous.^[46] Moreover, it reflects the spatial redistribution of material, leading to the transformation of the initially spherical particles into more realistic, irregular shapes for AM, SE, and CBD phases, thus enhancing the experimental relevance of the electrochemical model. The use of a meshing technique constitutes the second step for the importation of the electrode microstructures generated from the CGMD modeling workflow into our 4D-resolved mechano-electrochemical simulator. The voxelization and mesh generation were carried out with our in house software INNOV,^[47,48] which is used to voxelize and reconstruct multiphase volumetric meshes for FEM calculations.

It is worth noting that while the spherical particle hypothesis has been widely used to investigate electrochemical behavior due to its computational simplicity, it is inherently limited in representing realistic electrode microstructures. The 3D-resolved microstructure model adopted here allows for the inclusion of irregular particle geometries, polydispersity, and anisotropic connectivity of both solid and pore phases. These features are critical in governing localized ionic transport, current distribution, and mechanical stress concentrations, none of which can be adequately captured by idealized spherical approximations. Therefore, although more computationally intensive, the 3D framework provides a more accurate description of the electrode's multiphysics behavior and enables direct links between manufacturing-induced morphology and performance.

3.2. Coupling of the Solid Mechanics and Electrochemical Fields

The mesh was then imported into COMSOL Multiphysics software to build the 4D-resolved model for electrochemical and mechanical simulations. In this work, a half-cell model is built, which uses the 3D-resolved microstructure described in Section 2 as the cathode, SE as separator, Li metal as the anode, and Al as cathode current collector (CC). Then, a single discharge is simulated, which corresponds to the lithiation of the AM. All the calculations were performed in the Matrics platform (Université de Picardie Jules Verne)^[49] using one node with 500 GB of RAM and 1 processor (Intel Xeon CPU E5–2680 v4 @ 2.40 GHz, 28 cores).

3.2.1. Governing Equations

The diffusion of lithium inside the AM phase was assumed to follow the Fick's law^[50]

$$\frac{\partial c}{\partial t} + \nabla \cdot J = 0 \quad (1)$$

where c is the lithium molar concentration within the AM, t is the lithiation time, and J is the lithium flux inside the AM. The flux J is defined as a function of chemo-mechanical potential as^[51]

$$J = -\frac{D}{RT} c \nabla \mu \quad (2)$$

where D is the lithium diffusion coefficient inside the AM; R is the universal gas constant; T is the absolute temperature, and μ is the stress-dependent chemical potential, which can be defined by the hydrostatic stress (σ_h) as^[51]

$$\mu = \mu_0 + RT \ln X - \Omega \sigma_h \quad (3)$$

where μ_0 is the reference state potential, X is the molar fraction, and Ω is the partial molar volume. The third term on the left-hand side of Equation (3) results from the fully stress-concentration coupling. As we mentioned earlier, our study is focused on coupling concentration to strain/stress not the other way around, thus without stress-concentration coupling, the chemo-mechanical potential above reduces to^[52]

$$\mu = \mu_0 + RT \ln X \quad (4)$$

Combining Equations (2) and (3) the partial differential equation above reduces to^[52]

$$\frac{\partial c}{\partial t} - D \nabla^2 c = 0 \quad (5)$$

This intentional simplification allows us to isolate and analyze the mechanical response to electrochemical processes in a controlled and computationally tractable manner. While it neglects mechanisms such as stress-assisted lithium transport and its impact on kinetics, it provides valuable insight into stress evolution driven by intercalation and microstructural features. This mechanical foundational understanding at the mesoscale constitutes the basis for the development of more complete fully coupled models in our future work.

The diffusion-induced stress in the AM was solved by the following partial differential equation for mechanical equilibrium^[53]

$$\nabla \cdot \sigma + F_b = 0 \quad (6)$$

where σ is the Cauchy stress tensor and F_b is the body force. In this work, no body force was assumed, so $F_b = 0$.

The NMC811 material is considered to undergo a relatively modest volume expansion ($\approx 7\%$), and in the composite electrode environment, the surrounding carbon binder along with porosity and microstructural heterogeneity help limit effective strain levels.^[54,55] As a result, the majority of the AM is expected to remain within the elastic regime.^[18,56] Moreover, this assumption is

widely adopted in battery modeling studies, even for materials with much larger expansions like Silicon,^[57–60] as it enables analysis of stress evolution while keeping the computational cost manageable.

Even if the AM undergoes volume expansion with lithium insertion but the contribution of the deformation of SE and the CBD, as response to the AM expansion, to the whole electrode thickness change is non-negligible thus AM, SE, and CBD phases are treated as linear elastic materials. For elastic deformations during the charging/discharging process, the stress-strain relationship is governed by Hook's law as^[61]

$$\sigma = C : \varepsilon_e \quad (7)$$

where C is the elasticity tensor, and ε_e is the elastic strain. The total strain caused by the elastic and intercalation-induced deformations is given as^[61]

$$\varepsilon_t = \varepsilon_e + \varepsilon_{int} = \frac{1}{2} ((\nabla u)^T + (\nabla u)) \quad (8)$$

where ε_e and ε_{int} are the total and intercalation-induced strains, and u denotes the displacement field. Thus, the elastic strain is calculated by subtracting the intercalation-induced strain from the total strain as^[51]

$$\varepsilon_e = \varepsilon_t - \varepsilon_{int} \quad (9)$$

The intercalation-induced strain, which arises from lithium concentration changes during cycling, is formulated analogously to thermal strain in thermoelasticity^[62,63] and is given by

$$\varepsilon_{int} = \frac{1}{3} \Delta c \Omega I \quad (10)$$

where Δc is the concentration difference between the current and the initial state, and I is the identity matrix, and Ω is the partial molar volume of Lithium.

To calculate the concentration-dependent partial molar volume, the volume change data during the lithiation process of NMC811 were obtained from ref. [6], and it is shown in Figure 3b. The volumetric strain λ due to the volume change caused by the lithiation was calculated as

$$\lambda = \left(\frac{\Delta V}{V_0} + 1 \right)^{\frac{1}{3}} - 1 = \left(\frac{V_{x=x} - V_{x=x_{max}}}{V_{x=x_{max}}} + 1 \right)^{\frac{1}{3}} - 1 \quad (11)$$

where ΔV is the volume change that is calculated as the lithiation states increase. The $V_{x=x}$ is current, and $V_{x=x_{max}}$ is the initial (with minimum lithium content) unit cell volume. Based on this strain value, the partial molar volume Ω is given by

$$\Omega = \frac{3 \times \lambda}{(x - x_{max}) \times C_{total}} \quad (12)$$

3.2.2. Boundary and Initial Conditions

At the start of the simulation, it was assumed that minimum lithium concentrations c_{min} were homogeneously distributed throughout the NMC active particles as

$$c = c_{min} \text{ at } t = 0 \quad (13)$$

Figure 3a shows the boundary conditions and constraints given to the half-cell. Fixed support ($u = \theta_0$) for x , y , and z axes was applied at the external surface of the cathode CC. The green rectangles indicate fixed walls constraints, which were used to imitate the casing in actual ASSB implementation that may suppress the electrode expansion. An external pressure was applied at the external surface of the Li metal to keep the ASSB half-cell to mimic pressure applied by experimental casing.

The present study focuses on the mechanical evolution of the cathode under a half-cell configuration, which serves as a model system to decouple and systematically investigate the effect of cathode AM expansion without additional complexity introduced by full-cell interactions. Thus, we only focus on the effects of the expansion of the NMC811 phase on the displacements of the rest of electrode components. The separator and the CC were considered as rigid body domains, assuming that the effect of the deformation of the electrode induced by the expansion of NMC811 on both domains was negligible. Treating the SE as a rigid, nondeformable domain allows us to focus computational resources on the mechanical response within the active and composite phases,

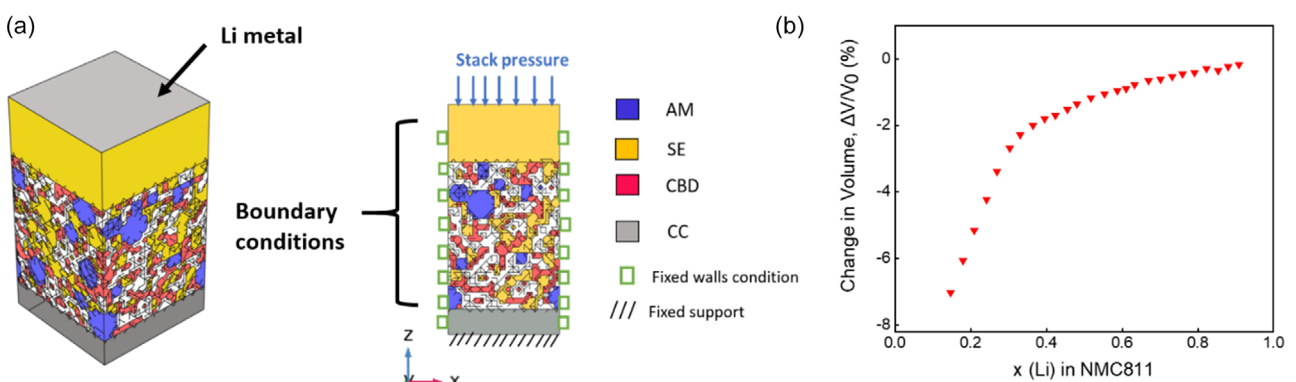


Figure 3. a) Simulated ASSB half-cell boundary conditions; b) predefined volume expansion field applied on the AM phase (NMC811). Figure produced with data from Ref. [6].

which are the main contributors to stress evolution in this configuration. The mechanical contribution of the SE will be addressed in our future work, where we plan to implement a fully coupled mechano-electrochemical model capable of capturing bidirectional interactions, including stress-assisted transport and the mechanical contribution of the SE phase. For simplicity, we proposed that other material properties, such as Young's modulus and diffusion coefficient of the AM, were independent of the lithium-ion concentrations. Other material properties and simulation parameters used in this work are listed in Table S1 and S2, Supporting Information.

The developed modeling framework is transferable and can be extended to other cathode chemistries and cell configurations by parametrizing the model accordingly.

4. Results and Discussions

4.1. Electrochemical Performance

To investigate the impact of mechanical constraints and material swelling on the electrochemical performance, FEM simulations were performed in COMSOL Multiphysics within a voltage window of 2.6–4.2 V versus Li⁺/Li. Three C-rates (C/5, C/10, and C/20) were evaluated under three modeling conditions: (i) no volume change, where lithiation-induced expansion of NMC811 was neglected and the electrochemical framework previously reported by group^[37] was applied; (ii) volume expansion with 9 MPa, incorporating the intrinsic volume change of NMC811 under the moderate stack pressure of 9 MPa; and (iii) volume change with 68 MPa, using the same expansion model under a high stack pressure of 68 MPa.

We selected to work with these two representative stack pressure values: 9 and 68 MPa, which were provided by our industrial research collaborators as typical operating bounds used in current R&D practice for ASSBs.

As shown in Figure 4, the overall differences in discharge voltage and capacity across the three scenarios are relatively small. This limited variation can be attributed to the one-way coupling approach adopted in this work, wherein electrochemical processes drive mechanical deformations, but the resulting mechanical stress and strain fields do not feed back into the electrochemical behavior. Consequently, while mechanical effects are pronounced in terms of stress evolution, their influence on the predicted electrochemical response remains minimal.

Nonetheless, a closer examination of the discharge curves reveals that higher stack pressure (68 MPa) more effectively suppresses the adverse effects of volume expansion, resulting in slightly improved capacity, especially at lower C-rates (Figure 4c). In contrast, the application of 9 MPa is not always sufficient to compensate for expansion-induced degradation, particularly during lithiation. These findings emphasize the need for a fully coupled mechano-electrochemical model that accounts for bidirectional interactions between electrochemical and mechanical fields to more accurately predict the performance and degradation behavior of ASSB cathodes.

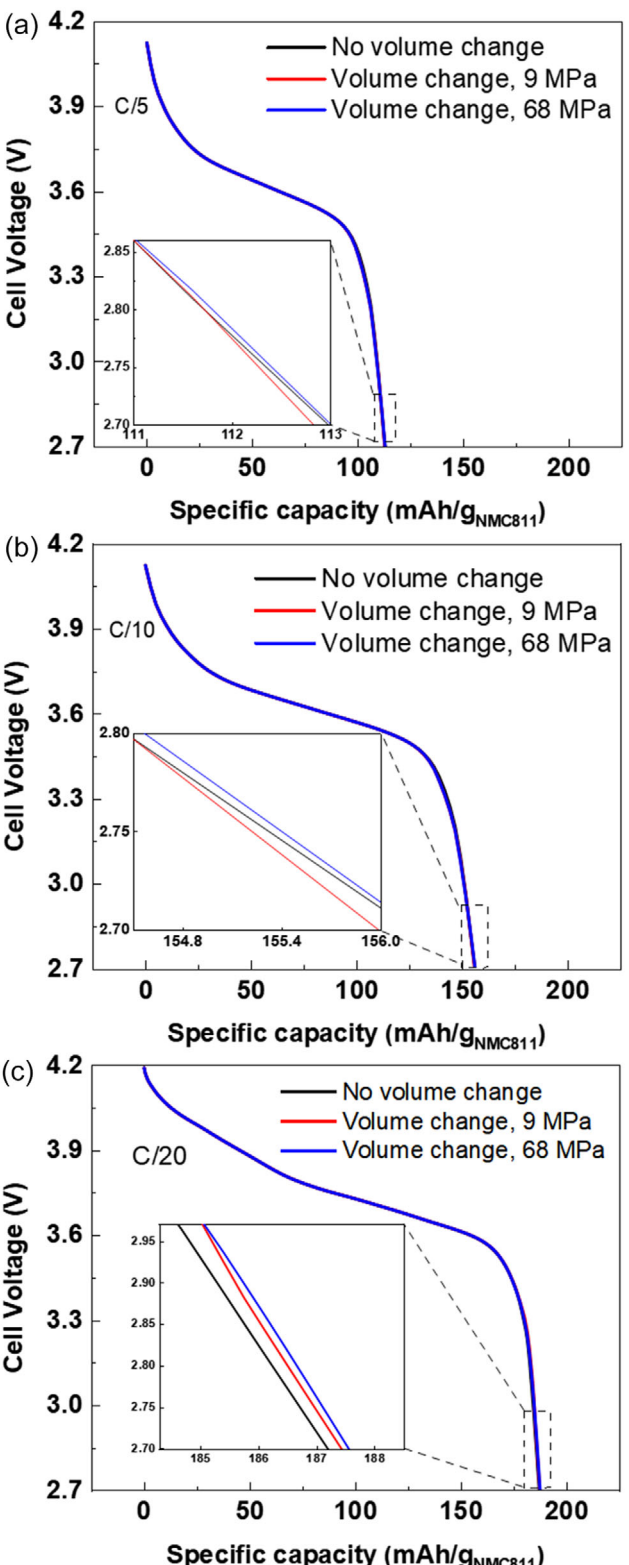


Figure 4. Calculated electrochemical performance of the ASSB half-cell at different C-rates: a) C/5, b) C/10, and c) C/20 for different cycling conditions.

Furthermore, Figure S1, Supporting Information, demonstrates the influence of volume expansion on electrode geometry and mesh deformation across the AM, SE, and CBD phases. At

a discharge rate of C/10 and under 9 MPa of applied pressure, the mesh is automatically refined by COMSOL based on the local strain field induced by the NMC811 expansion. This dynamic remeshing allows for accurate tracking of the evolving electrode morphology and enables a more realistic representation of the coupled electrochemical-mechanical behavior. These results highlight the necessity of accounting for volume changes in simulations of ASSB electrodes, especially when evaluating performance under practical cycling conditions and pressure constraints.

4.2. Battery Half-Cell Volume Expansion Behaviors under Different Charging Rates

Figure 5 presents the spatial distributions of lithium concentration, out-of-plane (z-direction) displacement, and von Mises stress within the NMC811 AM at the end of discharge for three different C-rates (C/5, C/10, and C/20), providing a detailed view of the mechano-electrochemical behavior under varying electrochemical conditions. At a higher C-rate of C/5, lithiation within the AM particles is highly nonuniform. The outer shell of the particles exhibits nearly complete lithiation, while the cores remain significantly less lithiated. This gradient in lithium concentration drives localized volumetric expansion predominantly near the particle surfaces, resulting in an overall displacement of approximately 0.43 µm, which corresponds to a 0.98% increase in electrode thickness relative to its initial state. In contrast, at the slower rate of C/20, lithium transport is more effective across the entire AM phase. This enables a more uniform lithiation profile both within

individual particles and across the electrode thickness, resulting in more homogeneous expansion. Under these conditions, the total z-direction displacement reaches 1.11 µm, corresponding to a 2.52% increase in electrode thickness.

The middle panels in Figure 5b further illustrate the displacement of the SE and CBD phases indicating strong mechanical coupling between the different phases within the composite cathode. The right panels (Figure 5c) show the corresponding von Mises stress distributions. At C/5, high stress concentrations appear in the outer regions of the AM particles, where lithium insertion and expansion are most intense. Conversely, at C/20, the stress field is more homogeneously distributed, consistent with the smoother lithiation and strain patterns. The complete change in lithium concentration and Von Mises stress during C/20 galvanostatic discharge is shown in the supplementary videos. This correlation stems from the fact that local mechanical stress arises from lithiation-induced strain gradients. Figure S2, Supporting Information, provides additional insight into the pressure field at C/5, where peak stress values reach up to 3 GPa, predominantly at the particle surfaces.

Figure 6 expands on the temporal and quantitative aspects of volume changes during discharge and with an applied stack pressure of 9 MPa. Figure 6b shows the evolution of out-of-plane (z) displacement of the separator which is equal to the change in thickness of the half-cell, while Figure 6d shows the corresponding cathode expansion ratio. Both metrics exhibit minimal change at early stages of discharge (DoD < 40%), regardless of the C-rate. This initial behavior reflects the elastic accommodation of lithium within the layered NMC811 structure, with limited structural

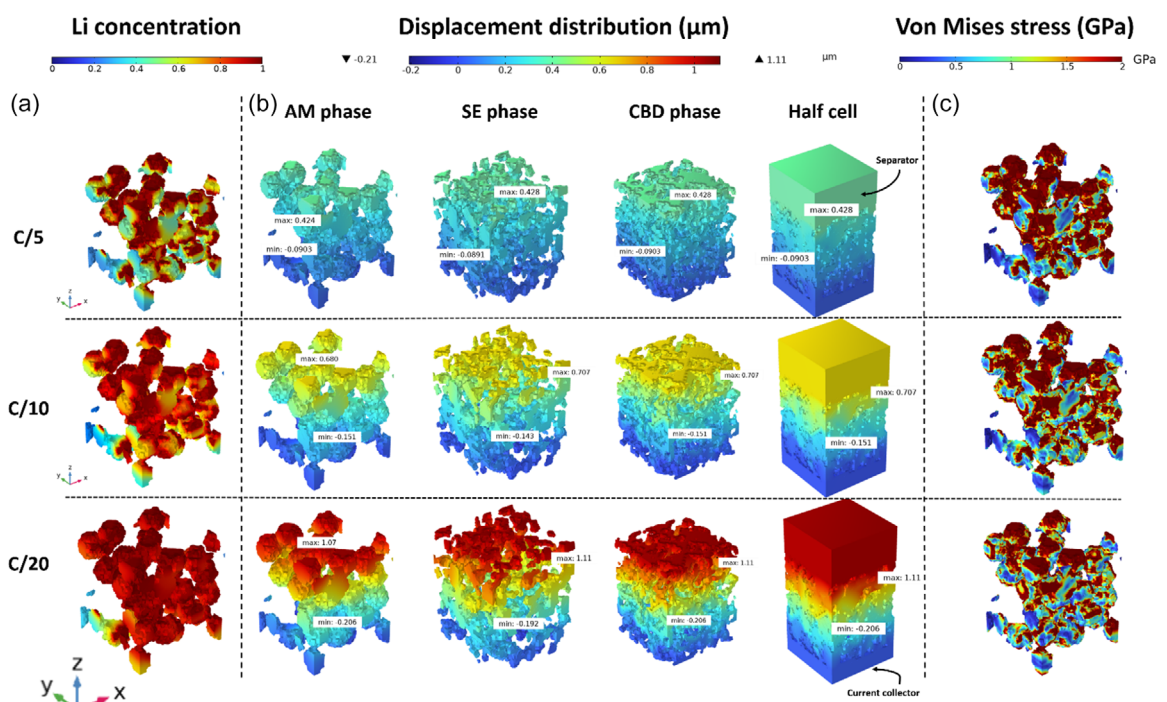


Figure 5. The spatial distribution of: a) Li concentration within NMC811; b) the displacement of different components within the composite cathode and within the global half-cell; and c) von Mises stress within the NMC811 phase for different C-rates and with an applied stack pressure of 9 MPa during discharge.

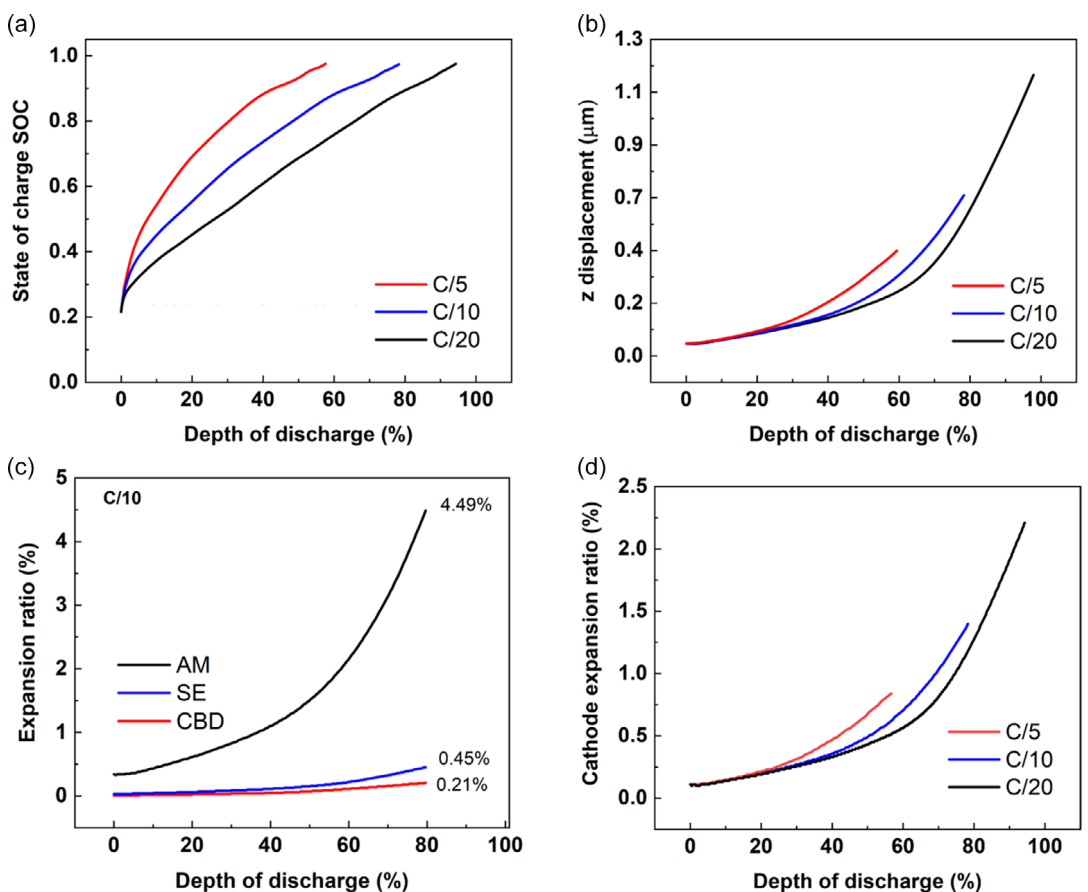


Figure 6. a) The evolution of the SOC for different C-rates; b) evolution of the separator displacement for different cycling rates; c) the evolution of the volume ratio for different phases in the cathode showing that the predominant contributor in the bulk deformation of the cathode is the AM; and d) evolution of the cathode expansion ratio for different C-rates. These results are under an applied stack pressure of 9 MPa.

perturbation. As discharge progresses ($\text{DoD} > 40\%$), the expansion becomes more pronounced and increasingly dependent on the C-rate. Interestingly, although faster cycling (e.g., C/5) results in more rapid lithiation near particle surfaces and thus higher local state of charge (SOC) (Figure 6a), the overall expansion is smaller. This is because high C-rates hinder lithium penetration into the particle cores, restricting full lithiation and resulting in lower global volume change. On the other hand, the C/20 case reaches the highest expansion: a total z-displacement of $\approx 1.2 \mu\text{m}$ and a cathode expansion ratio of $\approx 2.25\%$, reflecting nearly complete lithiation throughout the AM particles.

Figure 6c dissects the contribution of each phase to the total volume change at C/10. The AM exhibits the highest expansion, reaching 4.49% at $\approx 80\%$ DoD, due to lithium insertion. In contrast, the SE and CBD show insignificant volume increase (0.45% and 0.21%, respectively), primarily driven by mechanical deformation induced by the expanding AM. These results highlight the dominant role of AM in driving mechano-electrochemical changes in the composite cathode during galvanostatic operation and confirm that the bulk of the deformation is governed by lithium uptake in the NMC811 particles.

Overall, these results demonstrate a strong coupling between electrochemical kinetics, lithium distribution, and mechanical

deformation in ASSB cathodes. The degree of heterogeneity in both stress and strain fields is modulated by the applied C-rate, with lower rates promoting more uniform lithiation and thus greater total expansion. These insights are essential for optimizing mechanical stability and performance of composite electrodes under practical cycling conditions.

4.3. Impact of External Stack Pressure on Chemo-Mechanical Behavior during Discharge

Figure 7a illustrates the effect of external stack pressure on electrode volume change at the end of discharge across different C-rates. Under a low pressure of 9 MPa, the cathode exhibits pronounced thickness expansion, increasing by 0.78%, 1.61%, and 2.53% for C/5, C/10, and C/20, respectively. In contrast, applying a higher stack pressure of 68 MPa significantly suppresses this expansion due to enhanced particle packing and improved interfacial contact. At C/5, the high pressure nearly eliminates macroscopic swelling, even resulting in a slight contraction of 0.08%, indicating that mechanical confinement can mitigate internal expansion forces during fast cycling. For slower rates, the expansion is reduced but still present, reaching 0.74% at C/10 and 1.82% at C/20. These findings highlight the potential of optimized

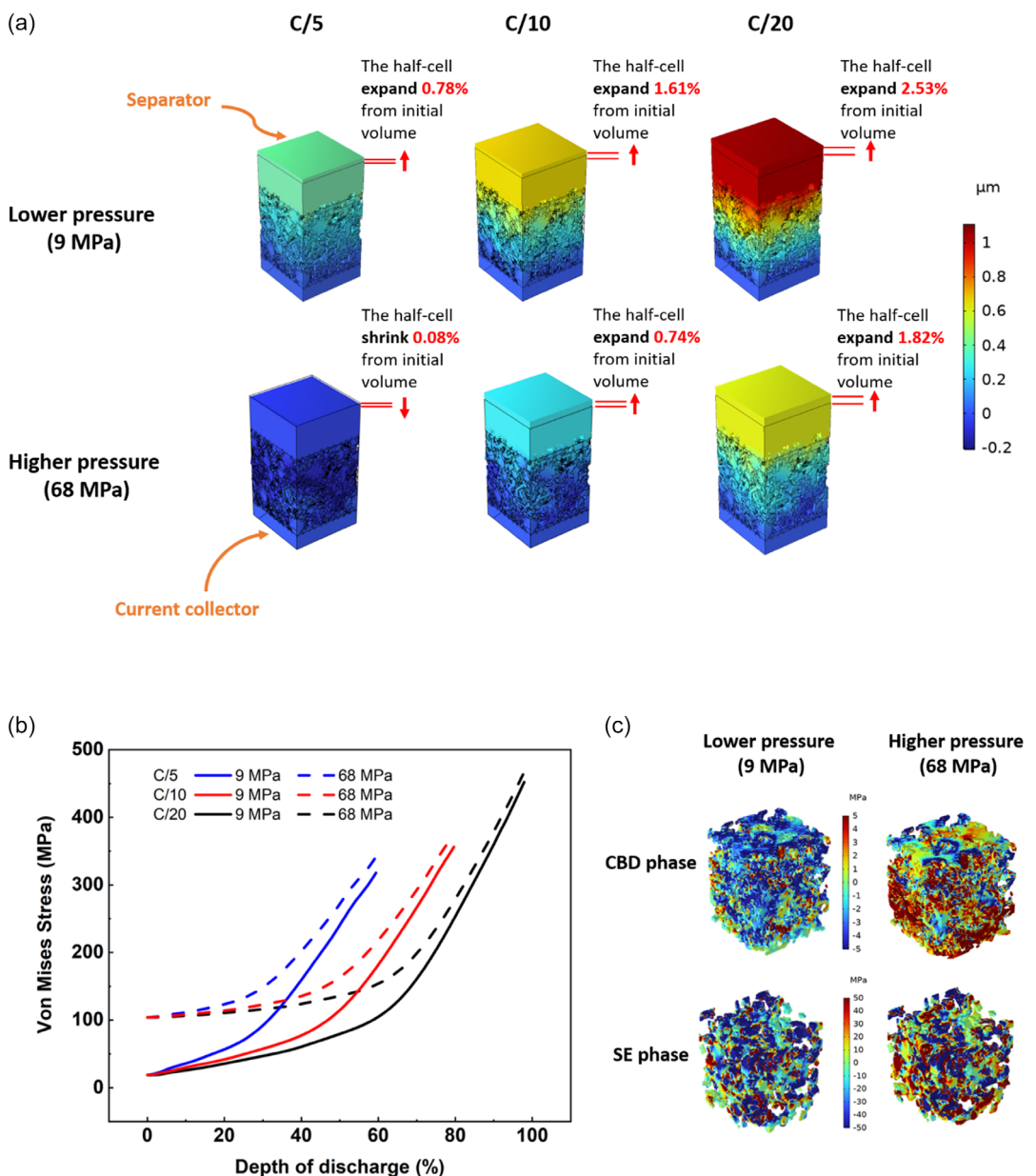


Figure 7. a) The impact of cycling stack pressure on the deformation of NMC half-cell and on the final thickness; b) the evolution of von Mises stress within the cathode for different C-rates and for different cycling conditions; and c) transition from tensile stresses to compressive stresses with increasing stack pressure within SE and CBD phases.

stack pressure to stabilize electrode morphology and suppress chemo-mechanical degradation in ASSBs.

Figure 7b presents the evolution of average von Mises stress within the NMC811 AM as a function of DoD, under both low (9 MPa, solid lines) and high (68 MPa, dashed lines) stack pressures. At all C-rates, von Mises stress increases with DoD, driven by the accumulation of internal strain resulting from lithium insertion-induced volume expansion. Higher C-rates (e.g., C/5) generate notably higher stresses than lower ones (e.g., C/20), particularly beyond 40% DoD, due to increased lithiation gradients and inhomogeneous strain development. These stress peaks stem from the fact that lithium preferentially inserts at

the particle surfaces under fast cycling, creating internal mismatches and localized deformation.

The application of 68 MPa stack pressure intensifies the von Mises stress across all C-rates. This stress amplification results from the mechanical constraint imposed by the external load, which resists free expansion and enforces tighter mechanical coupling among the composite phases. Although this constraint reduces overall electrode swelling, it increases the elastic energy stored in the AM particles, potentially elevating the risk of mechanical failure.

These observations emphasize the dual role of stack pressure in ASSB operation: while it promotes better interfacial

connectivity and suppresses macroscopic deformation, it also elevates internal stresses that may exacerbate particle fracture, delamination, or other degradation mechanisms, especially during high-rate cycling. Therefore, stack pressure must be carefully tuned to balance electrochemical performance and mechanical durability.

While the average von Mises stress provides an overall indicator of the mechanical state of AM, it is important to note that maximum stress values and the degree of stress heterogeneity may play a decisive role in local fracture initiation and mechanical degradation. These aspects highlight the importance of considering both global and localized stress metrics when assessing the mechanical reliability of the electrode.

Figure 7c shows the pressure fields within CBD and SE phases at the end of discharge under both pressure conditions. The pressure distributions exhibit a complex pattern of tensile (negative pressure) and compressive (positive pressure) regions. These heterogeneities arise from the mechanical response of the CBD and SE to the expansion of surrounding AM particles. Under tensile stress, the CBD and SE are vulnerable to cohesion loss, potentially leading to interfacial delamination from AM particles. Such detachment would compromise electronic percolation (via the CBD) or ionic conduction pathways (via the SE), impairing overall battery half-cell or cell performance. Conversely, excessive compressive stresses could cause local densification, which may hinder lithium transport through the compressed regions. An overall transition from tensile to compressive stresses is observed in the SE and CBD phases with increasing stack pressure.

Overall, these results demonstrate the importance of considering multiphase mechanical interactions when designing durable ASSL electrodes. While external pressure is necessary to maintain structural integrity and electrochemical connectivity, it must be optimized to minimize stress concentrations that could accelerate mechanical degradation over time.

5. Microstructural Changes

The primary mechanical influence on electrochemical performance has consistently been shown to arise from microstructural evolution during cycling.^[64,65] Key features affected include the interfacial surface area, porosity, tortuosity, and the resulting electronic and ionic conductivities. It is therefore essential in electrochemical-mechanical studies to discuss the indirect yet dominant role of mechanics on electrochemistry via microstructural changes at each step of cycling (Mechanics → Microstructure → Electrochemistry). Although this approach does not constitute a fully coupled framework, where mechanics directly enters the electrochemical equations through the inclusion of hydrostatic stress in the chemical potential or in the Butler-Volmer kinetics at interfaces,^[66] it still captures the crucial impact of microstructural evolution. In this section, three microstructural descriptors are examined in detail: interfacial area, porosity, and the tortuosity factor of the solid electrolyte phase.

5.1. Evolution of Interfacial Surface Area

As shown in Figure 8a,b, the specific interfacial areas at the AM-SE and AM-CBD contacts evolve with both stack pressure and DOD, relative to the reference state (no volume change).

At 20% DOD, both interfaces exhibit a substantial increase at 9 and 68 MPa, indicating that the initial volume change during lithiation promotes compaction and densification of the AM-SE interface regardless of the applied stack pressure.

At 40% DOD, the interfacial areas decrease at 9 MPa, reflecting a loss of AM-SE and AM-CBD contact due to the larger AM expansion. In contrast, at 68 MPa, the higher stack pressure restores interfacial contact, mitigating this loss.

At 60% DOD, the interfaces keep increasing under 68 MPa suggesting that the combined effect of AM expansion and applied stack pressure amplifies interfacial evolution through particle deformation of the AM, SE, and CBD phases. At 9 MPa, a modest increase is also observed relative to 40% DOD, consistent with the stabilized AM volume change (Figure 3b) and the supporting role of the applied pressure in maintaining interfacial contact.

Interestingly, the magnitude of change is less pronounced at the AM-CBD interface than at the AM-SE interface. This difference may be attributed to the more compliant carbon binder matrix, which can accommodate strain^[55] and partially buffer the mechanical effects of AM expansion. Nevertheless, both interfaces clearly exhibit a coupled dependence on pressure and DOD, underlining the critical role of electrochemical-mechanical interactions in dictating interfacial morphology and stability in ASSL composite cathodes.

Finally, the 3D renderings in Figure 8c highlight the morphological evolution of the AM-SE and AM-CBD interfaces at C/10 under different stack pressures. Increasing stack pressure results in denser, more compact interfacial geometries, consistent with the interfacial area trends and confirming the significant contribution of mechanical stress in restoring contact that would otherwise be lost during lithiation.

5.2. Pore Size Distribution

Figure 9 illustrates the evolution of the cumulative pore volume fraction as a function of mean pore diameter under three different conditions: (i) without accounting for NMC811 expansion, (ii) with NMC811 volume expansion under a low stack pressure of 9 MPa, and (iii) under a high stack pressure of 68 MPa. At 9 MPa, the applied mechanical constraint is insufficient to counteract the swelling induced by active material expansion. As a result, small and intermediate pores (0.2–2.6 μm) are significantly reduced and shifted toward smaller diameters, while larger pores (3–4.6 μm) are preserved. This evolution leads to a less uniform pore size distribution and therefore an increased microstructural heterogeneity.

In contrast, applying a higher stack pressure of 68 MPa mitigates the extent of expansion-induced deformation. The resulting cumulative curve closely resembles the no-expansion case within the intermediate pore size range (1.8–3 μm), suggesting the preservation of medium-sized pores. At the same time, the

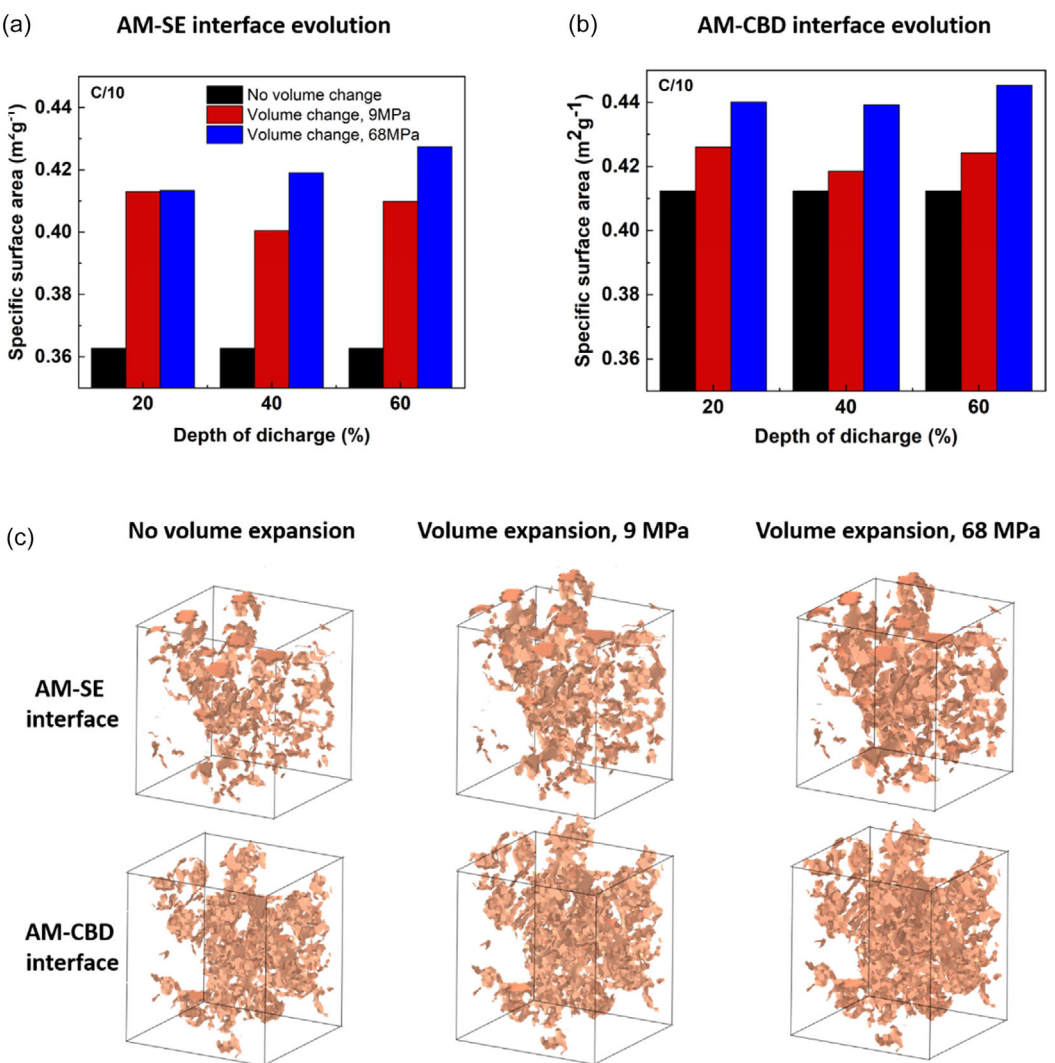


Figure 8. a,b) Evolution of AM-SE and AM-CBD interfacial specific surface areas in function of SOC and for different cycling conditions; and c) this graph shows the geometrical changes that occur for AM-SE and AM-CBD interfacial areas at C/10 after applying stack pressure (denser and more compact with increasing the stack pressure).

disappearance of larger pores ($>3\text{ }\mu\text{m}$) and the reduction in smaller pore volume fractions ($<=1.4\text{ }\mu\text{m}$) point to enhanced densification and homogenization of the pore network.

These results emphasize that volume expansion, if not properly constrained by external pressure, can significantly alter the pore size distribution, leading to increased heterogeneity in the microstructure. In contrast, applying sufficient compressive stress stabilizes the pore architecture promoting improved homogeneity, which is expected to facilitate more uniform ion and electron transport, thereby improving the electrochemical performance of the cathode. This interpretation aligns with the trends observed in Figure 8.

Furthermore, the observed microstructural trends are consistent with experimental findings reported in the literature,^[65,67] where increased compressive pressure resulted in higher AM volume fractions and reduced pore volume, further supporting the critical role of stack pressure in maintaining favorable electrode architecture throughout cycling.

5.3. Geometric Tortuosity

In ASSBs, the absence of liquid-phase buffering makes the tortuosity factor a critically important parameter, alongside the intrinsic ionic conductivity of SE. Figure 10 reports the geometric tortuosity (τ) of the SE phase, which quantifies the effective pathway length for Li^+ transport through the contiguous SE network. The calculations to determine the geometric tortuosity after a single discharge at C/10 were performed employing the DiffuDict module of GeoDict 2024 (Math2Market),^[68] using a standard desktop computer. The no-expansion case ($\tau = 7.736$) represents the baseline tortuosity of the electrode microstructure, unaffected by active material expansion or stack pressure. Under a moderate stack pressure of 9 MPa ($\tau = 8.182$), the electrode cannot sufficiently counteract the expansion of the AM. This expansion constricts SE pathways thereby increasing transport complexity and forcing ions to follow more convoluted paths. In contrast, at a high stack pressure of 68 MPa ($\tau = 7.765$), the

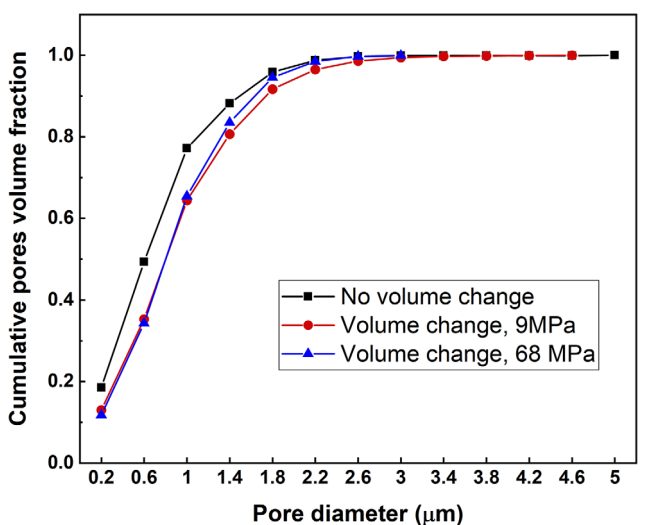


Figure 9. Cumulative pores volume fraction under different stress conditions at C/20: without volume change (black), with NMC811 volume expansion at 9 MPa (red), and at 68 MPa (blue).

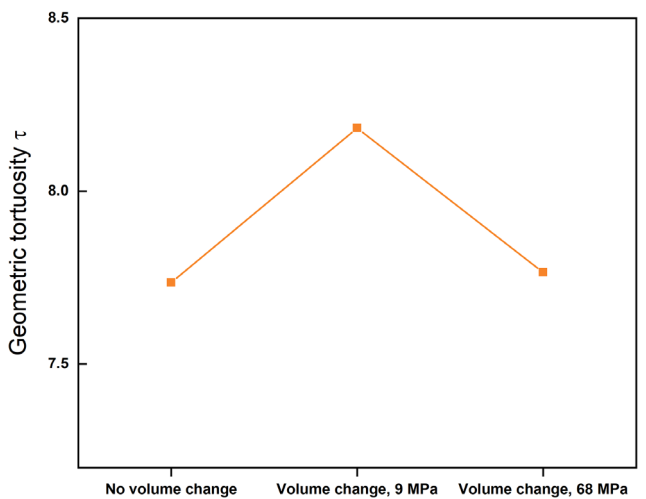


Figure 10. Geometric tortuosity of SE phase at the end of C/10 discharge at different cycling conditions.

mechanical constraint maintains interparticle contact and preserves SE continuity during lithiation. This stabilization prevents the formation of large local gaps (Figure 9), promotes a more homogeneous pore size distribution, and leads to denser interfacial surfaces at the AM–SE boundary (Figure 8). Consequently, the SE tortuosity remains close to the no-expansion baseline.

These results highlight the critical role of stack pressure in governing SE network connectivity, interfacial stability, and pore architecture, which collectively dictate the efficiency of ionic transport in composite cathodes.

6. Conclusions and Perspectives

In this work, we have presented the first steps towards a 4D-resolved computational modeling approach to understand the

electrochemistry-induced mechanical phenomena happening in ASSB composite electrodes starting from an electrode microstructure generated from a wet manufacturing process simulation using CGMD. We presented a computational workflow incorporating the ASSB NMC electrode microstructure generated by CGMD into an FEM simulator allowing to study how galvanostatic discharge impacts the mechanical behavior of the NMC composite electrode, given that NMC811 suffers a $\approx 7\%$ volume expansion upon lithiation. The electrochemistry, stress, and volume expansion behavior of a NMC811 half-cell were analyzed via this model. Then, the discharge conditions, such as the applied stack pressure upon discharge were discussed. The results indicated that the pressure constraint can change the structural arrangement of each phase in the half-cell, while it plays a very minor role in the electrochemical behavior. Furthermore, electrode deformation is highly dependent on the C-rate, directly influencing the overall half-cell volume change, the composite cathode thickness, and the average Von Mises stress distribution. Von Mises stress depicts greater accumulation of mechanical stress over time at lower C-rates which indicates higher mechanical deformation during complete lithiation.

Our model coupling electrochemistry and mechanics will help obtaining a more precise, and spatially resolved, understanding of the complex interplay between the electrochemical and mechanical behavior of NMC composite cathodes, eventually guiding the design of optimal electrode microstructures, and potentially unlocking the next generation of ASSB. We highlight that even if this model was designed for NMC811, it is transferable to other AM chemistries.

Furthermore, in this study and as proof of concept, we employed a one-way coupled linear framework to analyze the interplay between electrochemical and mechanical phenomena in ASSBs. The assumption of small deformations was justified based on the limited volumetric expansion of the AM relative to its particle size, allowing us to effectively model the system within a linear elasticity framework. However, to capture more complex mechanical behaviors such as plastic deformation, contact losses, and interfacial debonding, our future work will focus on developing a fully coupled nonlinear model that incorporates plasticity and more advanced constitutive laws to better describe the mechanical response of ASSB electrodes under cycling conditions. Our FEM computational model serves as a versatile and robust simulation framework designed to analyze the intricate processes involving electrochemistry and mechanics within batteries.

Supporting Information

The authors have cited additional references within the Supporting Information.^[69–70]

Acknowledgements

The authors declare having used ChatGPT (OpenAI) for an initial translation from French to English of some parts of the text which

was subsequently reviewed and significantly modified by the authors. S.B.H.A., V.S., and A.A.F. acknowledge the support by Umicore within the DESTINY PhD Program, which has received funding from the European Union's Horizon 2020 research and innovation program under the Marie Skłodowska-Curie Actions COFUND (grant agreement #945357). A.A.F. and M.A. acknowledge the European Union's Horizon Europe research and innovation program under grant agreement no. 101069686 (PULSEION). A.A.F. acknowledges Institut Universitaire de France for the support.

Conflict of Interest

The authors declare no conflict of interest.

Author Contributions

Siwar Ben Hadj Ali: conceptualization (lead); data curation (lead); formal analysis (lead); investigation (lead); methodology (lead); software (lead); visualization (lead); writing—original draft (lead).

Mohammed Alabdali: visualization (equal); writing—review & editing (equal). **Virginie Viallet:** funding acquisition (equal). **Vincent Seznec:** funding acquisition (equal); supervision (equal).

Alejandro A. Franco: conceptualization (lead); funding acquisition (lead); methodology (lead); project administration (lead); resources (lead); supervision (lead); writing—review & editing (lead).

Data Availability Statement

The data that support the findings of this study are available from the corresponding author upon reasonable request.

Keywords: composite cathodes · electrochemistry mechanics coupling · finite element method model · solid-state batteries · stack pressure impact

- [1] K. G. Gallagher, S. E. Trask, C. Bauer, T. Woehrle, S. F. Lux, M. Tschech, P. Lamp, B. J. Polzin, S. Ha, B. Long, Q. Wu, W. Lu, D. W. Dees, A. N. Jansen, *J. Electrochem. Soc.* **2016**, *163*, A138.
- [2] Y. Zhang, Y. Li, Z. Jia, Y. Liu, Y. Yu, L. Jiang, Q. Wang, Q. Duan, J. Sun, *J. Power Sources* **2024**, *620*, 235261.
- [3] K. Liu, Y. Liu, D. Lin, A. Pei, Y. Cui, *Sci. Adv.* **2018**, *4*, eaas9820.
- [4] S. P. Culver, R. Koerver, T. Krauskopf, W. G. Zeier, *Chem. Mater.* **2018**, *30*, 4179.
- [5] R. Koerver, I. Aygün, T. Leichtweiß, C. Dietrich, W. Zhang, J. O. Binder, P. Hartmann, W. G. Zeier, J. Janek, *Chem. Mater.* **2017**, *29*, 5574.
- [6] R. Koerver, W. Zhang, L. de Biasi, S. Schmidler, A. O. Kondrakov, S. Kolling, T. Brezesinski, P. Hartmann, W. G. Zeier, J. Janek, *Energy Environ. Sci.* **2018**, *11*, 2142.
- [7] D. Bistri, A. Afshar, C. V. Di Leo, *Meccanica* **2021**, *56*, 1523.
- [8] T.-Y. Yu, N.-Y. Park, H. Kim, I.-S. Lee, H.-J. Lee, K.-H. Kim, W. Cho, H.-G. Jung, K. Y. Chung, Y.-K. Sun, *ACS Energy Lett.* **2025**, *10*, 2477.
- [9] B.-K. Cho, S.-Y. Jung, S.-J. Park, J.-H. Hyun, S.-H. Yu, *ACS Energy Lett.* **2024**, *9*, 4068.
- [10] B. Aktekin, E. Kataev, L. M. Riegger, R. Garcia-Diez, Z. Chalkley, J. Becker, R. G. Wilks, A. Henss, M. Bär, J. Janek, *ACS Energy Lett.* **2024**, *9*, 3492.
- [11] E. P. Alsaç, D. L. Nelson, S. G. Yoon, K. A. Cavallaro, C. Wang, S. E. Sandoval, U. D. Eze, W. J. Jeong, M. T. McDowell, *Chem. Rev.* **2025**, *125*, 2009.
- [12] Y. Xiang, X. Li, Y. Cheng, X. Sun, Y. Yang, *Mater. Today* **2020**, *36*, 139.
- [13] D. H. S. Tan, A. Banerjee, Z. Chen, Y. S. Meng, *Nat. Nanotechnol.* **2020**, *15*, 170.
- [14] A. Neumann, T. R. Hamann, T. Danner, S. Hein, K. Becker-Steinberger, E. Wachsman, A. Latz, *ACS Appl. Energy Mater.* **2021**, *4*, 4786.
- [15] A. Neumann, S. Randau, K. Becker-Steinberger, T. Danner, S. Hein, Z. Ning, J. Marrow, F. H. Richter, J. Janek, A. Latz, *ACS Appl. Mater. Interfaces* **2020**, *12*, 9277.
- [16] S. B. H. Ali, M. Alabdali, V. Viallet, V. Seznec, A. A. Franco, *J. Power Sources* **2025**, *630*, 236131.
- [17] A. F. Bower, E. Chason, P. R. Guduru, B. W. Sheldon, *Acta Mater.* **2015**, *98*, 229.
- [18] A. M. Boyce, E. Martínez-Pañeda, A. Wade, Y. S. Zhang, J. J. Bailey, T. M. M. Heenan, D. J. L. Brett, P. R. Shearing, *J. Power Sources* **2022**, *526*, 231119.
- [19] D. Carlstedt, K. Runesson, F. Larsson, L. E. Asp, *Eur. J. Mech. A-Solids* **2022**, *94*, 104586.
- [20] T. Hofmann, D. Westhoff, J. Feinauer, H. Andrä, J. Zausch, V. Schmidt, R. Müller, *Int. J. Solids Struct.* **2020**, *184*, 24.
- [21] M. Magri, B. Boz, L. Cabras, A. Salvadori, *Electrochim. Acta* **2022**, *405*, 139778.
- [22] T. H. Wan, F. Ciucci, *Electrochim. Acta* **2020**, *331*, 135355.
- [23] B. Wu, W. Lu, *J. Mech. Phys. Solids* **2019**, *125*, 89.
- [24] Y. Zhao, R. Wang, E. Martínez-Pañeda, *J. Mech. Phys. Solids* **2022**, *167*, 104999.
- [25] T. Zhang, M. Kamlah, *J. Electrochem. Soc.* **2020**, *167*, 020508.
- [26] A. Timmons, J. R. Dahn, *J. Electrochem. Soc.* **2007**, *154*, A444.
- [27] L. Beaulieu, K. Eberman, R. Turner, L. Krause, J. Dahn, *Electrochim. Solid State Lett.* **2001**, *4*, A137.
- [28] Y. Bai, D. A. Santos, S. Rezaei, P. Stein, S. Banerjee, B.-X. Xu, *Int. J. Solids Struct.* **2021**, *228*, 111099.
- [29] G. Bucci, Y.-M. Chiang, W. C. Carter, *Acta Mater.* **2016**, *104*, 33.
- [30] Y. Liu, K. Guo, C. Wang, J. Han, H. Gao, *Int. J. Solids Struct.* **2020**, *198*, 99.
- [31] X. Zhang, A. Krischok, C. Linder, *Comput. Meth. Appl. Mech. Eng.* **2016**, *312*, 51.
- [32] F. Hao, W. Wang, P. P. Mukherjee, *J. Electrochim. Soc.* **2020**, *167*, 080513.
- [33] D. Bistri, C. V. Di Leo, *J. Electrochim. Soc.* **2021**, *168*, 030515.
- [34] Y. Huang, F. Zhang, Q.-A. Huang, Y. He, J. Zhang, *J. Electrochim. Soc.* **2021**, *168*, 120506.
- [35] X. Cai, Z. Guo, *J. Electrochim. Soc.* **2021**, *168*, 010517.
- [36] G. F. Castelli, L. von Kolzenberg, B. Horstmann, A. Latz, W. Dörfler, *Energy Technol.* **2021**, *9*, 2000835.
- [37] L. von Kolzenberg, A. Latz, B. Horstmann, *Batteries Supercaps* **2022**, *5*, e202100216.
- [38] M. So, T. Yano, A. Permatasari, V. L. Nguyen, G. Inoue, *Adv. Funct. Mater.* **2025**, 2423877.
- [39] H. Hanyu, Y. Bai, S. Benz, T. Weintraut, S. Wang, A. Henss, D. Raabe, J. Janek, *Adv. Mater.* **2025**, *37*, 2415006.
- [40] M. Alabdali, F. M. Zanotto, M. Chouchane, A. C. Ngandjong, V. Viallet, V. Seznec, Y. S. Meng, A. A. Franco, *Energy Storage Mater.* **2024**, *70*, 103527.
- [41] M. Alabdali, F. M. Zanotto, M. Duquesnoy, A.-K. Hatz, D. Ma, J. Auvergniot, V. Viallet, V. Seznec, A. A. Franco, *J. Power Sources* **2023**, *580*, 233427.
- [42] M. Alabdali, F. M. Zanotto, B. Notredame, V. Viallet, V. Seznec, A. A. Franco, *Batteries Supercaps* **2025**, *8*, e202400709.
- [43] LAMMPS Documentation (29 Aug 2024 version)—LAMMPS documentation, can be found under <https://docs.lammps.org/Manual.html> (accessed 30 September 2024), n.d.
- [44] T. Lombardo, F. Lambert, R. Russo, F. M. Zanotto, C. Frayret, G. Toussaint, P. Stevens, M. Becuwe, A. A. Franco, *Batteries Supercaps* **2022**, *5*, e202200116.
- [45] A. C. Ngandjong, T. Lombardo, E. N. Primo, M. Chouchane, A. Shodiev, O. Arcelus, A. A. Franco, *J. Power Sources* **2021**, *485*, 229320.
- [46] S. Pinilla, F. M. Zanotto, D. Z. Dominguez, T. García, A. A. Franco, *Energy Storage Mater.* **2024**, *74*, 103818.
- [47] M. Chouchane, A. A. Franco, *Batteries Supercaps* **2021**, *4*, 1375.
- [48] M. Chouchane, A. Rucci, A. A. Franco, *ACS Omega* **2019**, *4*, 11141.
- [49] Plateforme Matrics-Plateforme mutualisée pour les laboratoires de recherche de l'Université de Picardie Jules Verne, can be found under <https://www.matrics.u-picardie.fr/> (accessed 15 October 2024), n.d.
- [50] N. Iqbal, Y. Ali, S. Lee, *Electrochim. Acta* **2020**, *364*, 137312.
- [51] X. Zhang, W. Shyy, A. M. Sastry, *J. Electrochim. Soc.* **2007**, *154*, A910.
- [52] N. Iqbal, J. Choi, C. Lee, H. M. U. Ayub, J. Kim, M. Kim, Y. Kim, D. Moon, S. Lee, *Mathematics* **2022**, *10*, 4697.

- [53] P. Stein, A. Moradabadi, M. Diehm, B.-X. Xu, K. Albe, *Acta Mater.* **2018**, *159*, 225.
- [54] A. Lundkvist, P.-L. Larsson, A. H. S. Iyer, E. Olsson, *Powder Technol.* **2024**, *443*, 119873.
- [55] M. Han, H. Zhang, J. Wu, W. Zhang, C. Yuan, *J. Electrochem. En. Conv. Stor.* **2025**, *40*, 69379.
- [56] C. V. Di Leo, E. Rejovitzky, L. Anand, *J. Mech. Phys. Solids* **2014**, *70*, 1.
- [57] I. Tsagarakis, E. C. Aifantis, *Gradient Elasticity Effects on the Two-Phase Lithiation of LIB Anodes*, Vol. 90, Springer, Cham **2018**.
- [58] S. Golmon, K. Maute, S.-H. Lee, M. L. Dunn, *Appl. Phys. Lett.* **2010**, *97*, 033111.
- [59] P. Kargl, V. Drews, P. Daubinger, O. Schweighofer, M. Marinaro, G. A. Giffin, M. Wohlfahrt-Mehrens, A. Thaler, *J. Power Sources* **2022**, *548*, 232042.
- [60] C. Liu, O. Arcelus, T. Lombardo, H. Oularbi, A. A. Franco, *J. Power Sources* **2021**, *512*, 230486.
- [61] R. Xu, Y. Yang, F. Yin, P. Liu, P. Cloetens, Y. Liu, F. Lin, K. Zhao, *J. Mech. Phys. Solids* **2019**, *129*, 160.
- [62] I. Ryu, J. W. Choi, Y. Cui, W. D. Nix, *J. Mech. Phys. Solids* **2011**, *59*, 1717.
- [63] J. Christensen, J. Newman, *J. Solid State Electrochem.* **2006**, *10*, 293.
- [64] K. Taghikhani, W. Huber, P. J. Weddle, M. A. Zaeem, J. R. Berger, R. J. Kee, *J. Mech. Phys. Solids* **2025**, *198*, 106060.
- [65] Y. Sakka, H. Yamashige, A. Watanabe, A. Takeuchi, M. Uesugi, K. Uesugi, Y. Orikasa, *J. Mater. Chem. A* **2022**, *10*, 16602.
- [66] G. Bucci, T. Swamy, S. Bishop, B. W. Sheldon, Y.-M. Chiang, W. C. Carter, *J. Electrochem. Soc.* **2017**, *164*, A645.
- [67] M. Yamamoto, Y. Terauchi, A. Sakuda, A. Kato, M. Takahashi, *J. Power Sources* **2020**, *473*, 228595.
- [68] Case studies for battery materials - GeoDict Simulation Software, can be found under <https://www.math2market.com/geodict-applications/batteries.html> (accessed 30 September 2024), n.d.
- [69] B. A. Budiman, A. Saputro, S. Rahardian, M. Aziz, P. Sambegoro, I. P. Nurprasetio, *J. Energy Storage* **2022**, *52*, 104810.

Manuscript received: July 17, 2025

Revised manuscript received: September 10, 2025

Version of record online: